Study of the Structural, Vibrational and Thermodynamic Properties of Natroxalate Mineral Using Density Functional Theory

Francisco Colmenero[*] and Vicente Timón

Instituto de Estructura de la Materia, IEM-CSIC. C/ Serrano, 113. 28006 Madrid, Spain

Orcid Francisco Colmenero: https://orcid.org/0000-0003-3418-0735

Orcid Vicente Timón: https://orcid.org/0000-0002-7460-7572

[*] Corresponding author. Tel.+34 915616800 Ext. 941033
E-mail address: francisco.colmenero@iem.cfmac.csic.es

Abstract

Natroxalate mineral, $Na_2C_2O_4$, is a fundamental oxalate mineral widespread in nature, present in humans, animals and plants, as well as in naturally occurring minerals. The characterization of oxalate minerals is extraordinarily important since these organic minerals are indicators of environmental events and of the presence of biological activity, because they are commonly of biological origin. These minerals are currently under study to investigate the possible biological activity on Mars. The identification of these compounds is usually performed by X-ray diffraction and Raman spectroscopy. Theoretical calculations are of great value for the study and interpretation of the results of these experimental techniques. In this work, natroxalate mineral structure and Raman spectrum was studied by first principle calculations based on the density functional theory. The computed structure of natroxalate reproduces the one determined experimentally by X-ray diffraction (monoclinic symmetry, space group *P2₁/c*; lattice parameters *a*=3.449 Å, *b*=5.243 Å; *c*=10.375 Å). Lattice parameters, bond lengths, bond angles and X-ray powder pattern were found to be in very good agreement with their experimental counterparts. Raman spectrum was then computed by means of density functional perturbation theory and compared with the experimental spectrum. Since the results were also found in agreement with the experimental data, a normal mode analysis of the theoretical spectra was carried out and used in order to assign the main bands of the Raman spectrum. The band found at about 567 cm^{-1}, described as a single peak in previous experimental works, is shown clearly to have two contributing bands. Finally, two bands of the observed spectrum, located at the wavenumbers 1750 and 1358 cm^{-1}, were not found in the theoretical spectrum. This is because these bands correspond to an overtone, $2\nu_1$ (ν_1=875 cm^{-1}), and a combination band, $\nu_1+\nu_2$ (ν_1,ν_2 =875, 481 cm^{-1}), respectively. Finally, the fundamental thermodynamic properties of natroxalate mineral were determined. The calculated specific heat at 298.15 K is in excellent agreement with the experimental value, the difference being less than 1%. Since for most of these properties there are not experimental values to compare with, their values were predicted.

Keywords: Organic minerals, Oxalates, Natroxalate, DFT, Raman Spectroscopy

1. Introduction

Organic minerals have been recognized since the early stages of modern mineral science [1]. Most of these minerals are formed by inorganic processes, but it is increasingly recognized that minerals may also be produced organically. The recognition of the materials formed in this way has opened a new area of research, biomineralization, which is the study of the processes by which organisms produce minerals [2]. Because the occurrence of organic minerals is associated to high concentrations of certain organic compounds in natural environments, the study of the origin and formation processes of these minerals will lead us to understand the behavior of the organic molecules in the environment.

Oxalate minerals are fundamental organic minerals widespread in nature, present in humans, animals and plants [3-14], as well as in naturally occurring minerals [15-16]. The characterization of oxalate minerals is extraordinarily important since these minerals are indicators of environmental events, such as climate change [17], and of the presence of biological activity, because they are commonly of biological origin [2]. Evidence for the existence of primitive life forms like lichens and fungi can be based upon the formation of oxalates. These minerals form as the result of expulsion of heavy metals from fungi, lichens and plants [9-12], since these organisms can control their heavy metal intake through expulsion of metal salts such as oxalates. The production of simple organic acids as oxalic and citric acids has profound implications for metal speciation in biogeochemical cycles [12]. The presence of oxalates can be used as a marker for the pre-existence of life.

These minerals are currently under study to investigate the possible biological activity on Mars [18-27]. The study of the formation, transport, and concentration of oxalate in the extremely arid zones may provide a geochemical analogue for oxalate-bearing

minerals recently suggested to exist on Mars [18]. If life existed on Mars at some time in the past, or even exists in the present time, low life forms such as fungi and lichens could exist. These organisms may be found in very hostile environments [6-8]. Raman spectroscopy has been selected as one of the main analytical instruments for the ExoMars mission [19-20] to identify the geological and biogeological spectral signatures that could confirm the presence of oxalates in Mars. While there have been no inambiguous detections of specific organic compounds on Mars, meteoritic and cometary material is continuously delivered to the surface of Mars, and oxalic acid is the most abundant dicarboxylic acid in several chondrites [28-30]. Based on X-ray diffraction and reflectance spectroscopic analyses, Applin *et al.* [26-27] have shown that solid oxalic acid and its most common mineral salts are stable under the pressure and ultraviolet irradiation environment of the surface of Mars. Therefore, oxalate minerals could be important in numerous Martian geochemical processes, acting as a possible nitrogen sink, and/or contributing to the formation of organic carbonates, methane, and hydroxyl radicals [26].

The presence of oxalates has been evidenced by the deterioration of works of art [31-37]. Carbon dating of oxalic acid enables estimates of the age of the works of art [38]. Such minerals are also important in human physiology because these minerals are also found in the urinary system in the human body [3-5]. Oxalates are also used in industry [39-44]. For example, oxalates are major intermediates in many advanced oxidation processes for treating organics [40-43]. Sodium oxalate serves as a metal cleaning preparation in the textile, leather and tanning industries and it is also used in analytical and solvent extraction chemistry. For example, sodium oxalate is used as primary volumetric standard for manganometry and acidimetry [44].

The identification of these compounds is usually performed by X-ray diffraction and Raman spectroscopy. Theoretical calculations are of great value for the study and interpretation of the results of these experimental techniques since they may be used to resolve the main uncertainties encountered. The use of infrared and Raman spectroscopy for the study of oxalates originated with the necessity to study renal stones [45-46]. Vibrational spectroscopy has been extensively used to the study of oxalates [47-55,21-25] and many synthetic oxalates have been also studied [54-55]. Oxalates are most readily detected using Raman spectroscopy. Since most Raman spectra of oxalate minerals are mutually exclusive, these minerals may be adequately recognized with this kind of spectroscopy [21-25]. Therefore, Raman spectroscopy has the potential to identify the existence or pre-existence of life forms on planets such as Mars [21]. The minerals on Earth-like planets may be explored by robotic devices, which carry portable Raman spectrometers with possible fibre optics to collect spectral data.

The structure of natroxalate mineral phase has been determined by experimental X-ray diffraction techniques [56-57] and theoretical calculations [58-59]. In this paper, we performed a complete structural characterization of natroxalate by theoretical solid-state methods that agree very well with the structure obtained experimentally [56] and improves the one obtained theoretically [58]. Also, although the Raman spectrum of this mineral has been determined by experimental methods [21-23], a precise assignment of the main bands in the spectra is lacking. While the Raman spectrum of natroxalate was studied by Lakkaraju *et al.* [60] using DFT calculations of gas-phase clusters, these authors determined only two Raman bands, their assignment being taken from the experimental works. Therefore, a complete solid-state computation of the Raman spectrum of natroxalate mineral was carried out in this paper, including the computation of intensities and the assignment of all the observed bands. We have performed a

complete assignment of the experimental vibrational Raman bands since theoretical methods provide detailed views at the microscopic scale of the atomic vibrational motions in the corresponding normal modes. Finally, the fundamental thermodynamic properties of natroxalate mineral were determined. Since, as far as we know, the values for most of these properties of this mineral have not been determined by using either experimental or theoretical methods, their values were predicted in this work. Computations were carried out by means of Density Functional Theory [61] (DFT) based on plane waves and pseudopotentials [62]. The same methodology used successfully in previous works [63-67] was employed.

2. Methods

2.1. Geometries and Raman spectrum

CASTEP code [68], a module of the Materials Studio package [69], was employed to model natroxalate structure. The generalized gradient approximation (GGA) together with PBE functional [70] and Grimme empirical dispersion correction, called the DFT-D2 approach [71], were used. The introduction of dispersion corrections improved significantly the computed structural and vibrational properties as a result of the better description of non-bonded interactions among the atoms within the unit cell. The pseudopotentials used for C, O and Na atoms in the unit cell of natroxalate mineral were standard norm-conserving pseudopotentials [72] given in CASTEP code (00PBE-OP type).

Geometry optimization was carried out by using the Broyden–Fletcher–Goldfarb–Shanno optimization scheme [62,73] with a convergence threshold on atomic forces of 0.01 eV/Å. The kinetic energy cut-off and k-point mesh [74] must be selected to ensure good convergence for computed structures and energies. Natroxalate structure was optimized in calculations with increasing complexity by increasing these parameters.

The optimization performed with a cut-off of 900 eV and a K mesh of 6 x 4 x 2 (12 K points) gave a well converged structure that was used to determine the final results. Nevertheless, to show the convergence of the calculations, we have also included the structural results of the calculations with a large K mesh of $7 \times 5 \times 3$ (33 K points).

For the calculations of vibrational properties, the linear response density functional perturbation theory (DFPT) [75-77] implemented in the CASTEP code was used in the same way as in previous works [63-67]. Phonon frequencies at the gamma point of the Brillouin zone were computed using atomic displacement perturbations. Raman intensities are third-order derivatives of total energy with respect to vibrational mode (atomic position) and laser field (electric field, twice). These are calculated in CASTEP [68] by using a combination of perturbation theory (second derivative with respect to field) and finite differences (third derivative with respect to atomic displacement). Therefore, a combination of the DFPT and finite difference techniques are used in order to determine the Raman spectrum. The frequencies presented in this work have been scaled to correct for anharmonicity and remaining errors of the theoretical treatment employed, such as incomplete treatment of electron correlation and basis set truncation [78]. The scale factor used was 1.0363 and it was selected in order to adjust as far as possible the calculated Raman spectrum to the experimental one.

All the results reported in this work were obtained imposing monoclinic space symmetry (space group *P2₁/c*). However, the geometry optimization and vibrational calculations were also performed without symmetry restrictions. The results obtained in these last calculations were essentially the same as in the calculations in which the symmetry restrictions were imposed.

2.2. Thermodynamic properties

The methods employed for the calculation of thermodynamic properties of natroxalate were the same as in our previous works [65,67,79-80]. The phonon spectrum at the different points of Brillouin zone can be determined by DFPT as second order derivatives of the total energy [75]. Phonon dispersion curves and density of states were calculated and, from them, several important thermodynamic quantities in the quasi-harmonic approximation, such as free energies, enthalpies, entropies, specific heats and Debye temperatures were evaluated [75,81].

2.3. Enthalpies and free-energies of formation

The natroxalate enthalpies and free-energies of formation at different temperatures were determined from our calculated enthalpy and entropy functions, $(H_T - H_{298})^{calc}$ and S_T^{calc}, by using the relationships [82]:

$$\Delta_f H(T) = \Delta_f H^0 + (H_T - H_{298})^{calc} - \sum_i^{elements} n_i (H_T - H_{298})_i^{exp} \tag{1}$$

$$\Delta_f G(T) = \Delta_f H(T) - T \left\{ S_T^{calc} - \sum_i^{elements} n_i (S_T)_i^{exp} \right\} \tag{2}$$

In these relations, $\Delta_f H^0$ is the standard enthalpy of formation of natroxalate at the standard state (T = 298.15 K and P = 1 bar), and $(H_T - H_{298})_i^{exp}$ and $(S_T)_i^{exp}$ are the enthalpy and entropy functions of the elements forming part of this material with stoichiometric coefficients n_i, respectively. The specific value used for $\Delta_f H^0$ will be specified below. The enthalpy and entropy functions for the elements Na, C and O were taken form JANAF tables [82]. The equilibrium constants for the formation reactions were calculated using the well-known equation [82]:

$$\Delta G(T) = -R T \, Ln \, K \tag{3}$$

2.4. Enthalpies and free-energies of reaction

At the different temperatures, the enthalpies and free-energies of a given reaction were determined employing the calculated free energy and entropy of formation functions, $\Delta_f G(T)^{calc}$ and $\Delta_f S(T)^{calc}$, by using the relationships [82]:

$$\Delta_r G(T) = \sum_i^{products} n_i \Delta_f G^i(T) - \sum_j^{reactants} n_j \Delta_f G^j(T) \tag{4}$$

$$\Delta_r H(T) = \Delta_r G(T) + T \cdot \Delta_r S(T) \tag{5}$$

where:

$$\Delta_r S(T) = \sum_i^{products} n_i \Delta_f S^i(T) - \sum_j^{reactants} n_j \Delta_f S^j(T) \tag{6}$$

In equations (4) to (7), $\Delta_f G^i(T)$ and $\Delta_f S^i(T)$, are the free energy and entropy of formation at temperature T of the compound i forming part of the reaction with stoichiometric coefficient n_i. The thermodynamic data used for sodium carbonate and carbon monoxide, Na_2CO_3 and CO, were taken from JANAF tables [82]. The reaction equilibrium constants were determined, as in previous Subsection, in terms of the corresponding free energies of reaction by using equation (3).

3. Results and discussion

The unit cell parameters and internal atomic positions were first optimized using an initial atomistic model based in the atomic coordinates given by Reed and Olmstead [56]. From the optimized structure, we have obtained both the structural parameters as well as the X-ray powder pattern. Then, the vibrational Raman spectrum was predicted as a list of wavenumber and intensity values for each normal mode [77]. The experimental Raman spectrum was then compared with the computed one and the assignment of main fundamental band frequencies was carried out.

3.1. Structure

As it was mentioned, the structure of natroxalate was determined in calculations with increasing complexity. Table 1 gives the final lattice parameters, volumes and densities obtained compared with the experimental ones from Reed and Olmstead [56], Boldyreva *et al.* [58], Naumov [83], Khomyakov [84], and Swanson *et al.* [85]. The theoretical results of Boldyreva *et al.* [58] are also given in this table. As it can be seen, theoretical and experimental results are in very good agreement. The lattice parameters obtained with the large K mesh, including 33 k points, are essentially the same as those obtained with the smaller K mesh (12 k points). The errors in the computed volume and density with respect to experimental data are very small (less than 1%).

Table 1. Lattice parameters

Parameter	a (Å)	b (Å)	c (Å)	α	β	γ	Vol. (Å^3)	Dens. (g/cm^3)
Calc. - 12 k	3.4769	5.3205	10.2409	90	91.02	90	189.41	2.350
Calc. - 33 k	3.4769	5.3205	10.2409	90	91.02	90	189.41	2.350
DFT [58]	3.556	5.286	10.591	90	93.84	90	198.6	2.24
Exp. [56]	3.449	5.243	10.375	90	92.66	90	187.41	2.375
Exp. [58]	3.482	5.262	10.432	90	93.08	90	190.86	2.332
Exp. [83]	3.4847	5.2639	10.4360	90	93.08	90	191.15	2.329
Exp. [84]	3.479	5.255	10.426	90	93.14	90	190.32	2.339
Exp. [85]	3.4799	5.2552	10.420	90	93.10	90	190.29	2.340

The computed structure is shown in Figure 1, where a view of a 2 x 2 x 2 supercell along [100] is shown.
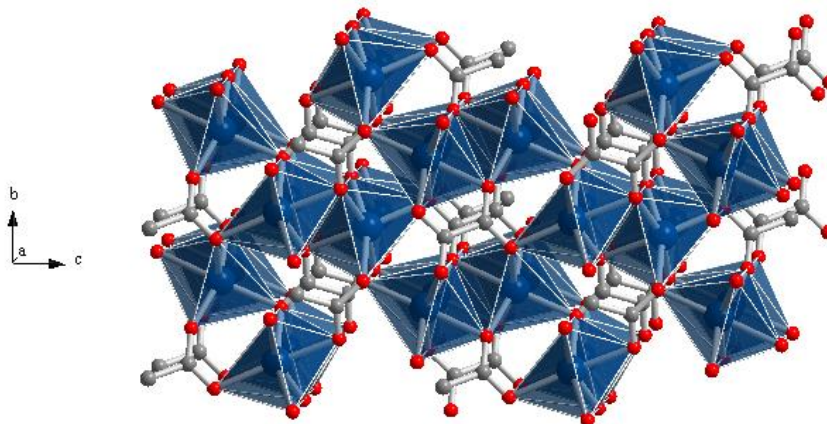

Figure 1. Structure of natroxalate mineral. View of a 2 x 2 x 2 supercell from the [100] direction. Color code: Na-Blue, C-Gray, O-Red.

As it can be seen, the structure is composed of isolated oxalate fragments, C_2O_4, coordinating the sodium atoms. The oxalate moiety is planar, as observed experimentally [56]. The sodium atoms are surrounded by six oxygen atoms from oxalate groups displaying octahedral coordination. A detailed description of oxalate mineral structures has been given by Echigo and Kimata [16,57].

Table 2 and Table 3 give a comparison of the more important geometric parameters (bond distances and angles) obtained with the corresponding experimental data from Reed and Olmstead [56]. Natroxalate unit cell contains only one structurally (symmetrically) identical Na atom, one C atom and two O atoms. The computed C-C, C-O1, C-O2 and O1-O2 distances within the oxalate fragment obtained using the smaller K mesh are 1.587, 1.262, 1.262 and 2.244 Å, which can be compared with the experimental distances of 1.567, 1.265, 1.253, and 2.241 Å, respectively. The structure of oxalate fragments is, therefore, very well reproduced (see also O1-C-O2, O1-C-C and O2-C-C bond angles in Table 3). Similarly, the coordination structure of Na ion is very well described, the average Na-O distance being 2.421 Å, which is comparable to the experimental value of 2.405 Å (see also the O-Na-O bond angles given in Table 3).

Table 2. Bond distances (in Å)

Bond	Exp. [56]	Calc. - 12 k	Calc. - 33 k
Oxalate fragment			
C-C	1.567	1.587	1.584
C-O1	1.265	1.262	1.263
C-O2	1.253	1.262	1.261
O1-O2	2.241	2.244	2.245
Octahedra around Na			
Na-O2	2.320	2.371	2.370
Na-O1	2.331	2.373	2.360
Na-O1'	2.343	2.376	2.372
Na-O2'	2.422	2.464	2.469
Na-O1''	2.495	2.451	2.467
Na-O2''	2.517	2.492	2.488
Average	2.405	2.421	2.421

Table 3. Bond angles (in deg)

Angle	Exp. [56]	Calc. - 12 k	Calc. - 33 k
Oxalate fragment			
O1-C-O2	125.74	125.47	125.60
O1-C-C	116.93	117.17	117.21
O2-C-C	117.33	117.36	117.19
Octahedra around Na			
O1-Na-O2	161.62	163.58	163.39
O1'-Na-O1	98.93	98.86	98.97
O2'-Na-O2	91.98	94.54	94.38
O1''-Na-O2	86.64	86.33	82.51
O2''-Na-O2	90.88	91.42	91.38
O2'-Na-O2''	80.09	82.56	82.82

The X-ray powder diffractogram of natroxalate was computed from the experimental [56] and computed structures (see the work by Downs *et al.* [86] for the method used in order to obtain the X-ray powder patterns from a given crystal structure) using CuK$_\alpha$ radiation (λ=1.540598 Å). The most intense lines (I > 10%) are compared in Figure 2, the agreement in line positions and intensities being very good. The use of the spectra derived directly from the experimental and computed structures allows for a fair comparison of the results free of interferences (as the experimental conditions) or possible artefacts (as the presence of impurities), since both are determined under identical conditions. Nevertheless, the use of an experimental pattern also leads to an excellent agreement. Computer program XPowder [87] using the PDF-2 database [88] recognizes the computed spectrum as that of natroxalate (pattern 48-1816, which corresponds to natural natroxalate mineral sample from Lovozero massif, Kola Peninsula, Russia, see Khomyakov [84]). The values of the main reflections obtained in our calculations are given in Table 4 and compared with those of the experimental patterns 48-1816 [84] and 20-1149 [85] of the PDF-2 database [88].

Table 4. Main reflections in the X-ray powder pattern of natroxalate: a) X-ray powder diffractogram computed from experimental geometry [56]; b) X-ray powder diffractogram computed from calculated geometry: 12 k point calculation; c) X-ray powder diffractogram computed from calculated geometry: 33 k point calculation; d) Experimental diffractogram (pattern 48-1816 from the PDF-2 database); d) Experimental diffractogram (pattern 20-1149 from the PDF-2 database).

| (a) Experimental [56]				(b) Calc. – 12 k			Calc. – 33 k			(d) Experimental [84]		(e) Experimental [85]	
2Θ (deg)	d (Å)	I (%)	[hkl]	2Θ (deg)	d (Å)	I (%)	2Θ (deg)	d (Å)	I (%)	d (Å)	I (%)	d (Å)	I (%)
55.440	1.6560	13.493	[0 3 2]	54.714	1.6763	14.269	54.730	1.6758	13.783	1.660	12	1.659	23
53.412	1.7140	10.631	[-1 1 5]	54.039	1.6956	10.481	54.349	1.6866	10.024	1.728	10	1.728	9
53.123	1.7226	9.076	[2 0 0]	52.538	1.7405	10.648	52.612	1.7382	9.457	1.770	4	1.768	8
50.420	1.8085	10.706	[-1 2 3]	50.325	1.8117	11.828	50.520	1.8051	11.172	1.822	7	1.820	11
47.392	1.8085	13.610	[1 2 2]	46.725	1.9425	16.084	46.649	1.9455	16.547	1.923	10	1.922	14
46.424	1.9544	7.138	[-1 -2 2]	46.131	1.9661	9.089	46.274	1.9604	9.011	1.968	6	1.966	7
44.504	2.0342	14.983	[1 2 1]	43.842	2.0633	14.870	43.813	2.0646	14.860	2.041	14	2.041	17
41.569	2.1708	16.197	[1 1 3]	41.159	2.1914	17.075	41.023	2.1984	17.698	2.177	13	2.176	17
38.735	2.3228	27.570	[0 1 4]	38.975	2.3090	25.065	39.016	2.3067	24.952	2.334	33	2.330	44
34.591	2.5910	31.219	[0 0 4]	34.982	2.5629	36.954	35.026	2.5598	36.032	2.602	56	2.600	56
31.909	2.8024	100.0	[-1 -1 1]	31.708	2.8197	100.0	31.816	2.8104	100.0	2.826	100	2.825	100
31.035	2.8793	16.183	[1 1 0]	30.667	2.9130	14.179	30.697	2.9102	13.858	2.898	27	2.985	31
30.975	2.8847	9.427	[0 1 3]	31.078	2.8754	10.685	31.107	2.8728	10.820	2.898	27	2.985	31
30.458	2.9325	8.301	[-1 0 2]	30.611	2.9182	11.348	30.807	2.9001	10.543	2.967	10	2.965	30
17.098	5.1819	10.285	[0 0 2]	17.286	5.1258	9.274	17.307	5.1196	8.591	5.203	13	5.202	24

13
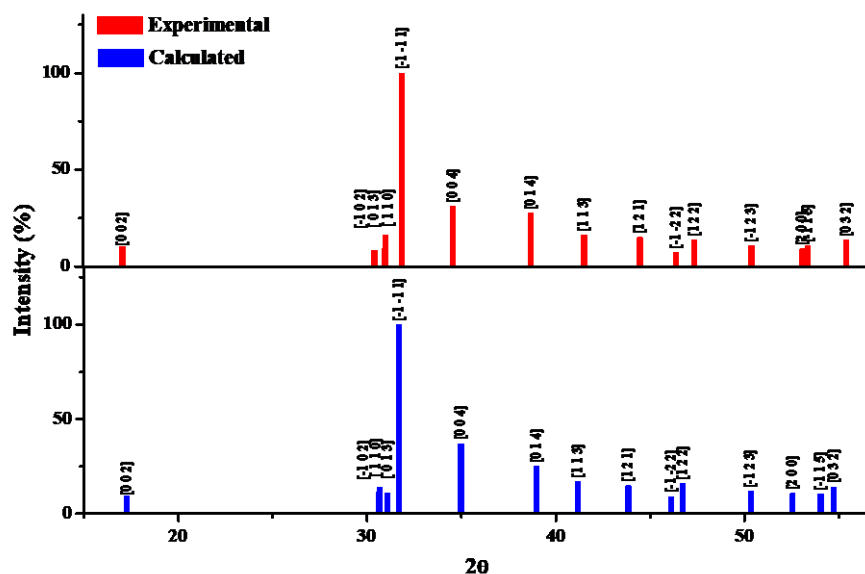
Figure 2. X-ray powder pattern of natroxalate using CuKα radiation: a) X-ray powder pattern computed from experimental geometry [56]; b) X-ray powder pattern computed from calculated geometry using the smaller K mesh (12 k points). The results for the main reflections are given in Table 4.

3.2. Raman spectra and band assignment

The theoretical Raman spectrum (computed at T=298 K, λ=532 nm and FWHM=20 cm^{-1}) in the wavenumber range of 1800-0 cm^{-1} is shown in Fig. 3. Pictures of the atomic motions in the most important Raman active vibrational modes are given in the Appendix A of the Supplementary Information (Fig. A.1).

In Fig. 4, we show the experimental [21-23] and theoretical Raman spectra divided in four regions: (A) 1800 to 1550 cm^{-1} (Fig. 4.A); (B) 1550 to1300 cm^{-1} (Fig. 4.B); (C) 1300 to 700 cm^{-1} (Fig. 4.C); and (D) 700 to 300 cm^{-1} (Fig. 4.D). Note that the wavenumber range showed in Fig. 4.C is only 1000-750 cm^{-1} (as shown in Fig. 3, there are not Raman bands in the remainder of region C). The wavenumber of both spectra along with the corresponding calculated intensities and assignments are given in Table 5. This table includes also the low wavenumber region 300-0 cm^{-1}. The numerical values of the experimental Raman shifts given by Frost *et al.* [21] are provided in this

table with the aim of comparison. The results obtained in each region will be now discussed.
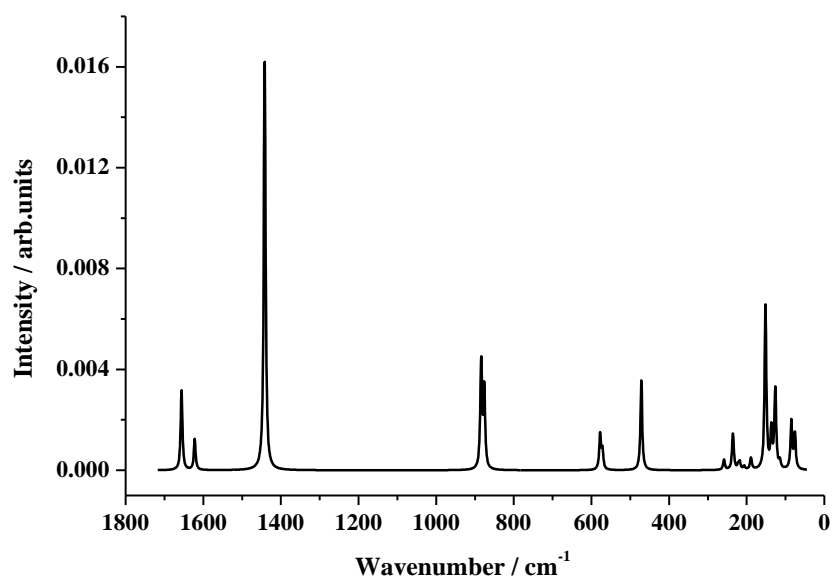

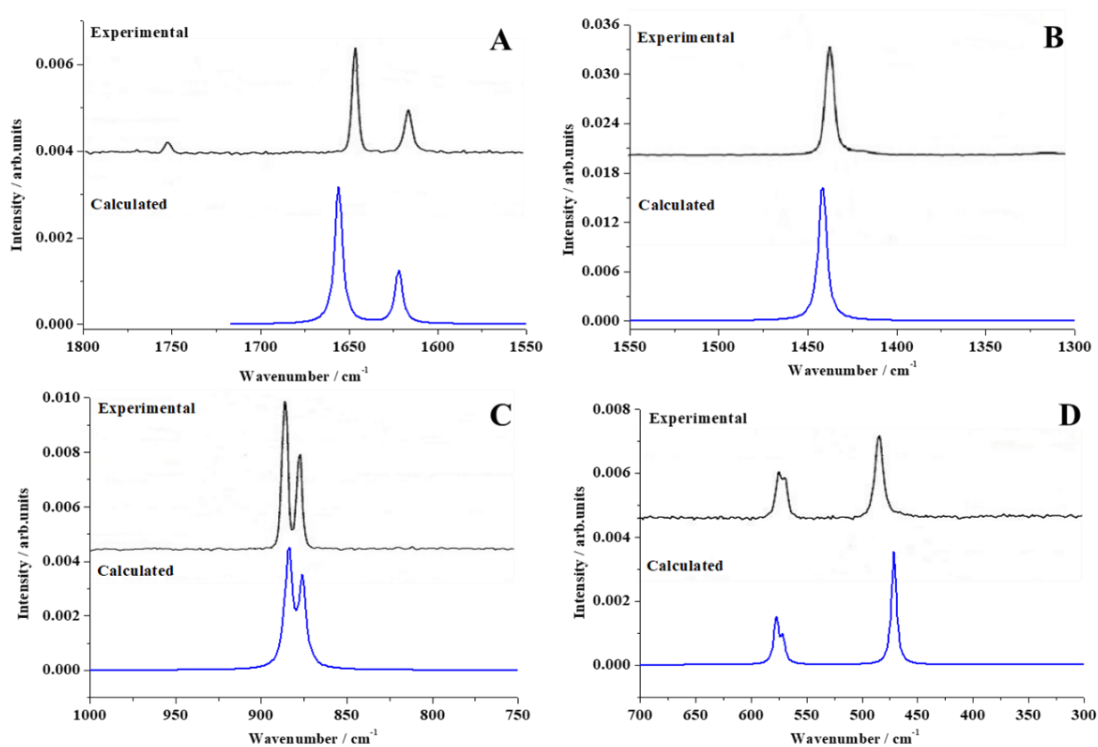**Figure 3.** Calculated Raman spectra of natroxalate mineral.

Figure 4. Experimental [21] and theoretical Raman spectra of natroxalate mineral. (A) Region: 1800-1550 cm^{-1}; (B) Region: 1550-1300 cm^{-1}; (C) Region: 1300-700 cm^{-1}; (D) Region: 700-300 cm^{-1}.

(A) *1800 to 1550 cm^{-1} region*

In this region, we found one intense band at about 1643 cm^{-1} and a weaker band at 1614 cm^{-1}. The corresponding computed Raman shifts are 1656 and 1622 cm^{-1}. The symmetries of the corresponding vibrations are Bg and Ag, respectively. These two bands are assigned to antisymmetric CO bond stretching vibrations, $\nu^a(CO)$. The band observed by Frost *et al.* [21] at 1750 cm^{-1} does not appear in the calculated spectrum. It is likely that this band is an overtone, $2\nu_1$ (ν_1=875 cm^{-1}). The band located at 875 cm^{-1} is described below (1000 to 750 cm^{-1} region).

(B) *1550 to 1300 cm^{-1} region*

In this region, we find a single band which is the most intense in the whole Raman spectrum and it is located at 1456 cm^{-1} (Ag). The corresponding calculated Raman shift is 1442 cm^{-1}. This band is assigned to antisymmetric CC bond stretching vibrations plus symmetric CO bond stretching vibrations, $\nu^a(CC) + \nu^s(CO)$. For comparison, Lakkaraju *et al.* [60] using DFT gas-phase cluster calculations, obtained a Raman shift for this band of 1444 cm^{-1}. The weak intensity band observed by Frost *et al.* [21] at 1358 cm^{-1} does not appear in the calculated spectrum. This band seems to be a combination band, $\nu_1+\nu_2$ (ν_1, ν_2 =875, 481 cm^{-1}). The bands placed at 875 and 481 cm^{-1} are described below.

(C) *1300 to 700 cm^{-1} region*

There are two observed bands in this region with wavenumbers 884 and 875 cm^{-1}, which correspond to the bands calculated at 884 and 876 cm^{-1}. The first of these bands has larger intensity than the second one. The corresponding vibrations to these bands have Ag symmetry in both cases. The first of these bands is assigned to symmetric CC bond stretching vibrations plus OCO bending vibrations $\nu^s(CC) + \delta(OCO)$. The

second one is assigned to oxalate fragment deformation vibrations. The assignment of the first band is the same as that given by Frost *et al.* [21]. These authors attributed the second band to a splitting of the CC bond stretching vibrations in the free oxalate fragment due to non-equivalence of the CC stretching vibrations. However, these authors gave not a proper assignment of this band since the associated vibrational motion was not described. The motion involves a CC bond rotation, where C atoms move perpendicularly to oxalate plane but in opposite directions (see Figure A.1 of the Supplementary Information). Lakkaraju *et al.* [60] obtained a Raman shift for the first of these bands of 884 cm^{-1}.

(D) *700 to 300 cm^{-1} region*

While Frost *et al.* [21] report two bands within this region of the Raman spectrum at 567 and 481 cm^{-1}, a simple inspection of Figure 4.D shows that the first one contains two contributing peaks. The theoretical calculation is able to resolve these peaks, and we find three bands in this region at wavenumbers 578, 572 and 471 cm^{-1}. The calculated spectrum in this region is in very good agreement with the observed one, as it can be seen in Fig. 4.D. The above three bands correspond to vibrations of symmetry Bg, Ag and Ag, respectively. The first two bands are assigned to oxalate fragment deformation vibrations. The motion in these vibrations involves a CC bond rotation, where C atoms move within the oxalate plane but in opposite directions. The third band is attributed to CO_2 group translations within the oxalate plane.

(E) *Low wavenumber 300 to 0 cm^{-1} region*

In this last region, we may observe the presence of three main weak bands at wavenumbers 221, 156 and 117 cm^{-1} with theoretical counterparts of 235, 152 and 126 cm^{-1} (symmetries Ag, Bg and Ag, respectively). These vibrations were assigned in the experimental work [21] to out of plane bending vibrations. The theoretical treatment

allows to specify that the first band may be ascribed to CO_2 group translations out of the

oxalate plane. The second and third ones are both assigned to OCO twisting vibrations.

Table 5. Experimental and calculated Raman band wavenumbers, calculated intensities and assignments.

Exp. Raman shift (cm^{-1}) [21]	Calc. Raman shift (cm^{-1})	Irr. Rep. (C$_{2h}$)	Int. (Å^4)	Assignment
1800 -1550 cm^{-1} region				
1760	-	-	-	$2\nu_1$ (ν_1=875 cm^{-1})
1643	1655.9	Bg	51.77	$\nu^a(CO)$
1614	1622.0	Ag	21.44	$\nu^a(CO)$
1550-1300 cm^{-1} region				
1456	1442.0	Ag	204.51	$\nu^a(CC) + \nu^s(CO)$
1358	-	-	-	$\nu_1{+}\nu_2$ (ν_1, ν_2 =875, 481 cm^{-1})
1300-700 cm^{-1} region				
884	884.0	Ag	34.53	$\nu^s(CC) + \delta(OCO)$
875	876.0	Ag	24.42	$\varrho(C_2O_4)$
700-300 cm^{-1} region				
567	577.7	Bg	7.08	$\varrho(C_2O_4)$
-	571.6	Ag	3.65	$\varrho(C_2O_4)$
481	471.3	Ag	12.38	$T^{ip}(CO_2)$
Low wavenumber region				
221	235.4	Ag	2.78	$T^{op}(CO_2)$
156	151.6	Bg	7.74	$t(OCO)$
117	126.3	Ag	3.13	$t(OCO)$

3.3. Thermodynamic properties

3.3.1. Phonon dispersion and density of states

   Phonon calculations were performed at the optimized structure of natroxalate. From

them, the thermodynamic properties were evaluated. The calculated phonon dispersion

curves and the density of states spectrum obtained in the calculations performed with

the smaller K mesh (12 K points) are displayed in Figure 5. The results obtained with

the larger K mesh involving 33 K points are almost indistinguishable from the results of

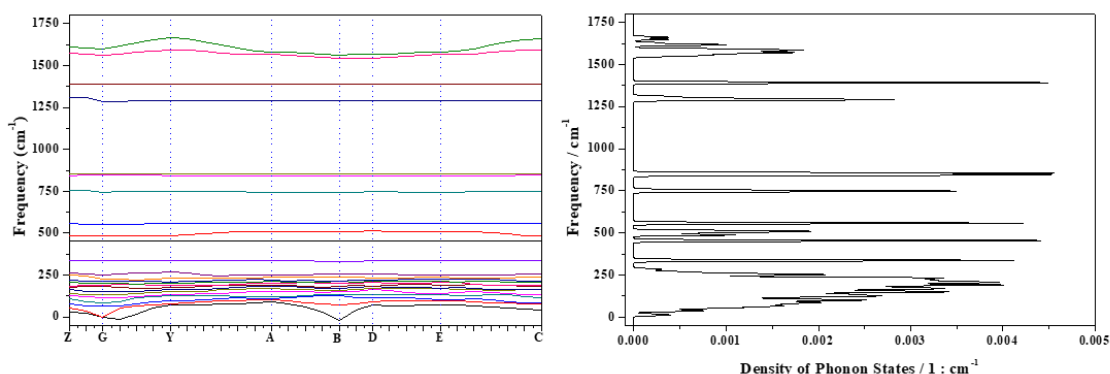the smaller calculations at the scale used in Figure 5.

Figure 5. Calculated phonon dispersion curves and density of states spectrum obtained by using the smaller K mesh (12 k points).

3.3.2. Heat capacities, entropies, enthalpies and Gibbs free energies

Figures 6.A, 6.B, 6.C and 6.D show the calculated isobaric heat capacity, entropy, enthalpy and free energy functions, respectively. Note that all enthalpy and free energy values have been divided by the temperature to express these properties in the same units as entropy and heat capacity ($J \cdot K^{-1} \cdot mol^{-1}$). The values of the calculated themodynamic functions over the temperature range 0-900 K are given in Table 6.

The knowledge of the thermodynamic properties of sodium oxalate is relevant for the study of Bayer process [89]. A comparison of the calculated specific heat values of natroxalate at 298.15 K and 281 K with the experimental values reported in references [89] and [90], respectively, is given in Table 7. As it can be seen, the agreement with the experimental values is excellent, the errors being less than 1%. The last value of the calculated heat capacity, at the temperature of 900 K, is 182.2798 $J \cdot K^{-1} \cdot mol^{-1}$, which is below the Dulong-Petit limit, 199.54 $J \cdot K^{-1} \cdot mol^{-1}$, by 8.6%. In Table 7, the computed value of the entropy at 298.15 K is also compared with the experimental value reported in the literature [91]. The agreement is again very good, but it must be

19

noted that this value is not for natroxalate crystal but for sodium oxalate as electrolyte in solution.
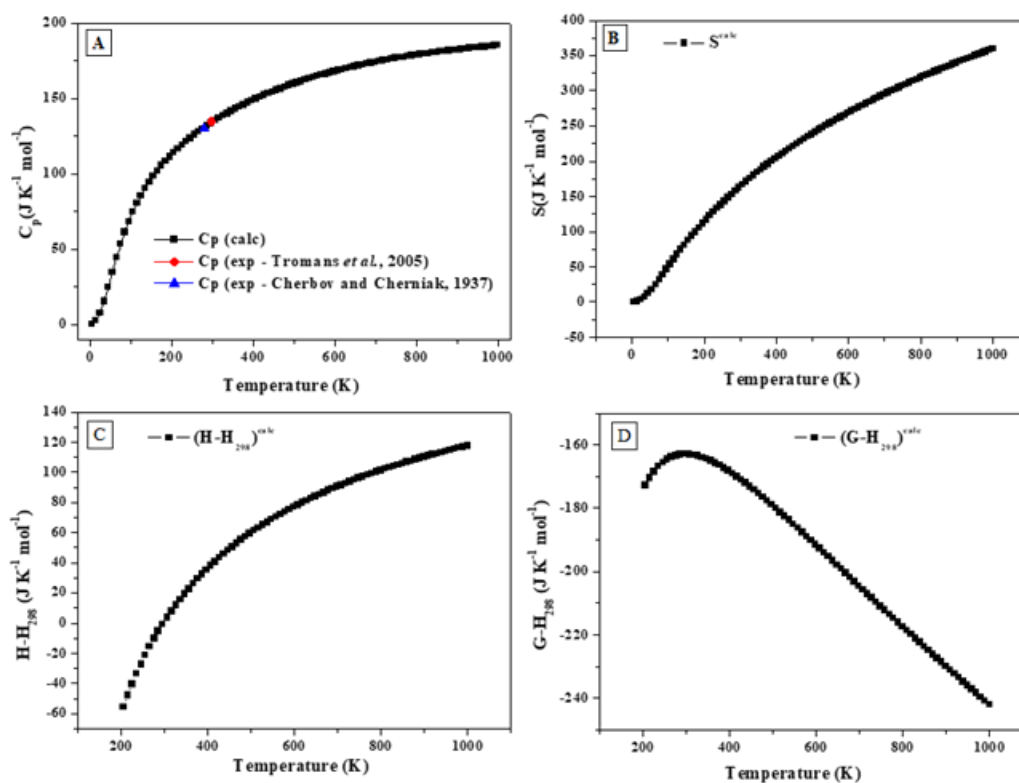

Figure 6. Calculated thermodynamic properties of natroxalate mineral: A) Isobaric specific heat; B) Entropy; C) Enthalpy; D) Gibbs free energy. All functions are given as a function of temperature.

Table 6. Calculated isobaric heat capacity, entropy, enthalpy and free energy functions of natroxalate mineral. All values are in units of $J \cdot K^{-1} \cdot mol^{-1}$.

T(K)	C_p^{calc}	S^{calc}	$(H-H_{298})^{calc}$	$(G-H_{298})^{calc}$
298.15	133.7039	162.9526	0.0	-162.9944
360.00	143.4783	189.0893	23.8654	-165.2226
380.00	146.2376	196.9220	30.2379	-166.6821
400.00	148.8297	204.4890	36.0979	-168.3888
420.00	151.2687	211.8086	41.5137	-170.2929
440.00	153.5665	218.8974	46.5425	-172.3535
460.00	155.7336	225.7703	51.2320	-174.5377
480.00	157.7792	232.4405	55.6218	-176.8191
500.00	159.7114	238.9200	59.7444	-179.1769
520.00	161.5371	245.2197	63.6269	-181.5947
540.00	163.2627	251.3491	67.2917	-184.0599
560.00	164.8937	257.3172	70.7573	-186.5625
580.00	166.4351	263.1318	74.0396	-189.0946
600.00	167.8918	268.8003	77.1523	-191.6498

620.00	169.2681	274.3294	80.1076	-194.2228
640.00	170.5681	279.7253	82.9165	-196.8087
650.00	171.1908	282.3751	84.2694	-198.1051
700.00	174.0511	295.1693	90.5675	-204.5990
800.00	178.6979	318.7226	101.2899	-217.4334
900.00	182.2798	339.9881	110.1022	-229.8855

Table 7. Comparison of calculated and experimental heat capacities and entropies of natroxalate. All values are given in units of $J \cdot K^{-1} \cdot mol^{-1}$.

T	Exp.	Calc.	Error (%)
	Isobaric Heat Capacity		
298.15	134.6 ± 2.24 [89]	133.7039	-0.7
281	130.0 [90]	130.6029	0.5
	Entropy		
298.15	163.6 [91]	162.9526	-0.4

3.3.3. Enthalpies and Gibbs Free energies of formation

The thermodynamic properties of natroxalate, reported in previous Section, were used to determine the enthalpies and free energies of formation of natroxalate as a function of temperature using the same methods as in our previous works [79-80]. This procedure has produced very accurate thermodynamic properties of formation for uranyl containing materials even at high temperatures. For example, for rutherfordine mineral and gamma uranium trioxide [79], the theoretical results were shown to be in excellent agreement with experimental information up to 700 K and 900 K, respectively. From the calculated thermodynamic properties of natroxalate, the experimental values of the thermodynamic properties of Na, C, and O atoms from Chase *et al.* [82] and the experimental value for the standard enthalpy of formation given by Wagman *et al.* [91], $\Delta_f H^0 = -1318.0$ kJ/mol, we obtained the enthalpies and free-energies of formation and reaction constants of natroxalate as a function of temperature given in Table 8. The results are also displayed in Figure 7.

Table 8. Calculated enthalpies ($\Delta_f H$) and free-energies ($\Delta_f G$) of formation and reaction constants (Log K) of natroxalate as a function of temperature. The values of $\Delta_f H$ and $\Delta_f G$ are in units of kJ·mol^{-1}.

| T(K)	$\Delta_f H$	$\Delta_f G$	Log K
5	-6237.880633	-6237.688883	65163.033549
55.2525	-1725.551058	-1710.235679	1616.781689
105.5051	-1496.121818	-1459.178361	722.408291
206.0101	-1362.065747	-1287.763476	326.509017
298.15	-1318.000000	-1210.149666	212.007810
360	-1302.604803	-1172.514908	170.123168
400	-1296.196093	-1151.672479	150.389178
500	-1287.931568	-1107.347593	115.680871
600	-1286.693667	-1070.242655	93.170536
700	-1290.030538	-1037.897045	77.446862
800	-1296.516093	-1008.825351	65.867865
900	-1305.459788	-982.322091	57.011043
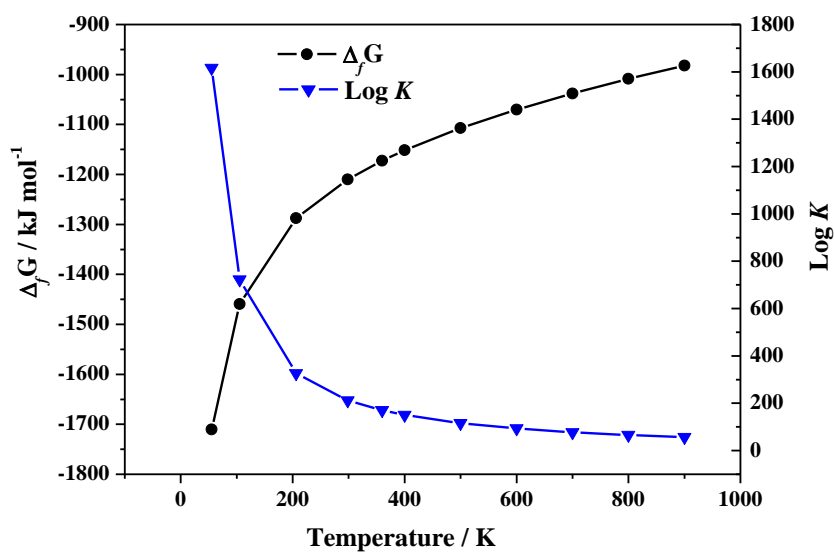
Figure 7. Calculated free-energies of formation and reaction constants of natroxalate as a function of temperature.

3.3.4. Thermal decomposition of natroxalate

Since sodium oxalate is used as starting material for versatile industries, it is very important to study its thermal decomposition for advantages in cost and time

22

management for industrial production. The reaction of thermal decomposition of natroxalate into sodium carbonate and carbon monoxide is:

$$Na_2C_2O_4 \rightarrow Na_2CO_3 + CO \qquad (1)$$
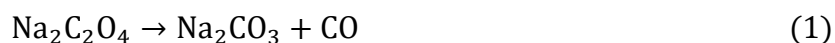
From the thermodynamic properties of natroxalate, reported in the previous sections and the experimental ones of sodium carbonate and carbon monoxide given in JANAF tables [82], we obtained the enthalpies, free-energies and reaction constants of this reaction as a function of temperature reported in Table 9, using the same methods as in our previous work [80]. The results are also displayed in Figure 8. Present results of the thermodynamic properties of this important reaction of thermal decomposition complement the previous kinetic studies performed by several authors [92-94]. The decomposition temperature of sodium oxalate was placed at about 290ºC (563 K) in previous experimental studies [94]. As it may be appreciated in Figure 8, the calculated free energy of reaction becomes negative at a temperature of 84ºC (357.3 K) and, therefore, the sodium oxalate crystalline material (natroxalate) appears to start to decompose already at lower temperatures. It must be noted that although the Gibbs free energy of reaction becomes negative at this temperature, the decomposition reaction is very slow at low temperatures [92]. Therefore, the large difference in the experimental and calculated decomposition is probably due to the very slow kinetic rate of this reaction. Finally, it should be noted that in the work by Yoshimori *et al.* [94], reporting the decomposition temperature of sodium oxalate, nothing was pointed about the crystallinity of the samples studied.

Table 9. Calculated enthalpies ($\Delta_r H$), free-energies ($\Delta_r G$) and associated reaction constants (Log K) of the reaction of thermal decomposition of natroxalate as a function of temperature. The values of $\Delta_r H$ and $\Delta_r G$ are in units of kJ·mol^{-1}.

T(K)	$\Delta_r H$	$\Delta_r G$	Log K
5	4999.936084	4999.849330	-52231.740915
55.2525	486.613072	479.607804	-453.400151
105.5051	254.420059	237.398527	-117.530981
206.0101	120.172268	85.135482	-21.585876
298.15	83.055490	24.977666	-4.375872

360	62.312913	-0.927404	0.134559
400	55.986893	-14.035521	1.832804
500	49.992568	-38.466407	4.018456
600	52.097267	-56.069345	4.881146
700	60.415138	-69.517955	5.187362
800	70.363693	-80.372649	5.247662
900	81.827588	-88.950909	5.162445
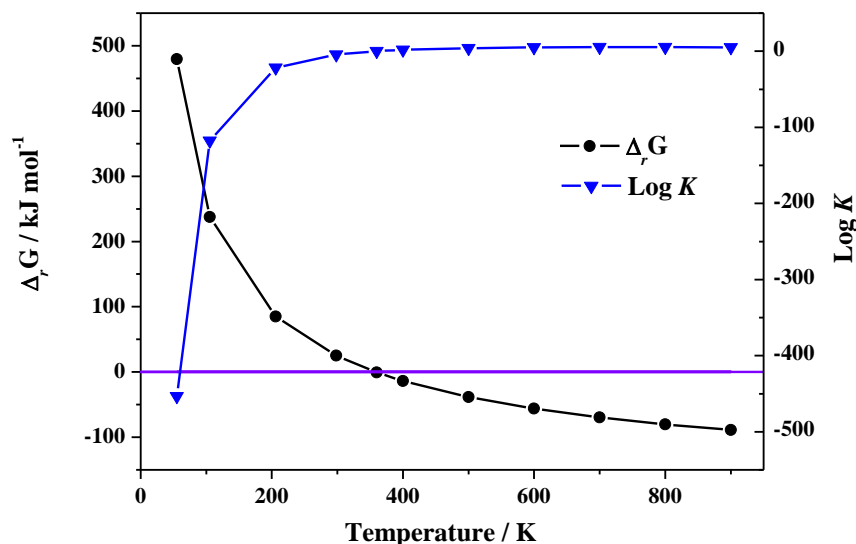
Figure 8. Calculated free-energies and reaction constants of the reactions of thermal decomposition of natroxalate mineral as a function of temperature.

4. Conclusions

Natroxalate mineral, $Na_2C_2O_4$ was studied by first principle calculations based on the density functional theory. The computed structure of natroxalate reproduced accurately the one determined experimentally by X-ray diffraction. Lattice parameters, bond lengths, bond angles and X-ray powder pattern were found to be in very good agreement with their experimental counterparts.

The Raman spectrum was then computed by means of density functional perturbation theory and compared with the experimental spectrum. Since the results were also found in agreement with the experimental data, a normal mode analysis of the theoretical spectra was carried out and used in order to assign the main bands of the Raman

spectrum. The procedure allowed assigning rigorously all observed bands including those at very low wavenumbers. The main bands used to fingerprint this mineral are those associated to the Raman shifts placed at 1643, 1456, 884 and 481 cm^{-1}, and were reproduced theoretically at 1656, 1442, 884, and 471 cm^{-1}, respectively. They were assigned to antisymmetric CO bond stretching vibrations, antisymmetric CC bond stretching vibrations, symmetric CC bond stretching plus OCO bending vibrations, and CO_2 translations within the oxalate plane, respectively. The band observed at about 567 cm^{-1}, described as a single peak in the experimental works, was shown clearly to have two contributing peaks. Finally, it must be noted that two weak intensity bands of the observed spectrum [21], located at wavenumbers 1750 and 1358 cm^{-1}, were not found in the theoretical spectrum. This is because these bands correspond to an overtone, $2\nu_1$ (ν_1=875 cm^{-1}), and a combination band, $\nu_1+\nu_2$ (ν_1, ν_2 =875, 481 cm^{-1}), respectively.

The fundamental thermodynamic properties of natroxalate mineral were also theoretically determined. The calculated specific heat at 298.15 K was in excellent agreement with the experimental value, the difference being less than 1%. The enthalpies and free-energies of formation of natroxalate as well as the enthalpies and free-energies of its reaction of thermal decomposition were also reported as a function of temperature.

Since DFT method has been found to be a reliable tool to analyze the structure and vibrational spectra of natroxalate, this methodology may also be used to obtain a deeper knowledge of the structure, spectra and properties of other very important organic minerals and compounds found under extreme environmental conditions, such as those found on Mars.

Acknowledgements

SUPPLEMENTARY DATA

Supplementary data associated with this article are included in Appendix A, where pictures of the atomic motions in the Raman active vibrational modes of natroxalate mineral are given.

References

[1] B. Mason, L. G. Berry, Elements of Mineralogy, W. H. Freeman, San Francisco, California, 1968.

[2] S. Weiner, P. M. Dove, An overview of biomineralization processes and the problem of the vital effect, Rev. Mineral. Geochem. 54 (2003) 1-29.

[3] J. A. Wesson, M. D. Ward, Pathological biomineralization of kidney stones, Elements 3 (2007) 415-421.

[4] R. Selvaraju, A. Raja, G. Thiruppathi, FT-Raman spectral analysis of human urinary stones, Spectrochim. Acta A 99 (2012) 205–210.

[5] J. P. Pestaner, F. G. Mullick, F. B. Johnson, Calcium oxalate crystals in human pathology: molecular analysis with the laser Raman microprobe, Arch. Pathol. Lab. Medicin. 120 (l996) 537-540.

[6] H. G. M. Edwards, N. C. Russell, M. R. D. Seward, Calcium oxalate in lichen biodeterioration studied using FT-Raman spectroscopy, Spectrochim. Acta A 53 (1997) 99-105.

[7] H. G. M. Edwards, N. C. Russell, M. R. D. Seaward, D. Slarke, Lichen biodeterioration under different microclimates: an FT Raman spectroscopic study, Spectrochim. Acta A 51 (1995) 2091-2100.

[8] H. G. M. Edwards, J. M. Holder, D. D. Wynn-Williams, Comparative FT-Raman spectroscopy of Xanthoria lichen-substratum systems from temperate and antarctic habitats, Soil Biol. Biochem. 30 (1998) 1947–1953.

[9] H. J. Arnott, M. A. Webb, The structure and formation of calcium oxalate crystal deposits on the hyphae of a wood rot fungus, Scan. Electron Microsc. (1983) 1747-1758.

[10] J. E. Chisholm, G. C. Jones, O. W. Purvis, Hydrated copper oxalate, moolooite, in lichens, Mineral. Mag. 51 (1987) 715-718.

[11] A. Frey-Wyssling, Crystallography of the two hydrates of crystalline calcium oxalate in plants, Am. J. Bot. 68 (1981) 130-141.

[12] G. M. Gadd, Heterotrophic solubilization of metal-bearing minerals by fungi, Mineral. Soc. Ser. 9 (2000) 57-75.

[13] T. Wadsten, R. Moberg, Calcium oxalate hydrates on the surface of lichens, Lichenol. 17 (1985) 239-245.

[14] P. V. Monje, E. J. Baran, Characterization of calcium oxalates generated as biominerals in cacti, Plant Physiol. 128 (2002) 707-713.

[15] B. A. Hofmann, S. M. Bernasconi, Review of occurrences and carbon isotope geochemistry of oxalate minerals: implications for the origin and fate of oxalate in diagenetic and hydrothermal fluids, Chem. Geol. 149 (1998) 127–146.

[16] T. Echigo, M. Kimata, Crystal Chemistry and Genesis of Organic Minerals: A Review of Oxalate and Polycyclic Aromatic Hydrocarbon Minerals, Can. Mineral. 48 (2010) 1329-1358.

[17] S. Moore, M. J. Beazley, M. R. McCallum, J. Russ, Can calcium oxalate residues from lichen activity reflect past climate change? Preprints of Extended Abstracts presented at the ACS National Meeting, American Chemical Society, Division of Environmental Chemistry 40 (2000) 4-5.

[18] Z. Y. Cheng, D. C. Fernández-Remolar, M. R. M. Izawa, D. M. Applin, M. Chong Díaz, M. T. Fernandez-Sampedro, M. García-Villadangos, T. Huang, L. Xiao, and V. Parro, Oxalate formation under the hyperarid conditions of the Atacama Desert as a mineral marker to provide clues to the source of organic carbon on Mars, J. Geophys. Res. Biogeosci. 121 (2016) 1593-1604.

[19] H. G. M. Edwards, I. B. Hutchinson, R. Ingley, N. R. Waltham, S. Beardsley, S. Dowson, S. Woodward, The search for signatures of early life on Mars: Raman spectroscopy and the Exomars mission, Spectrosc. Eur. 23 (2011) 6-15.

[20] F. Rull, J. Martinez-Frias, Raman spectroscopy goes to Mars, Spectrosc. Eur. 18 (2006) 18-21.

[21] R. L. Frost, Y. Jing, Z. Ding, Raman and FTIR spectroscopy of natural oxalates: Implications for the evidence of life on Mars, Chin. Sci. Bull. 48 (2003) 1844-1852.

[22] R. L. Frost, A. Locke, W. N. Martens, Raman spectroscopy of natural oxalates at 298 and 77 K, J. Raman Spectrosc. 34 (2003) 776-785.

[23] R. L. Frost, Raman spectroscopy of natural oxalates, Anal. Chim. Acta 517 (2004) 207-214.

[24] R. L. Frost, A. J. Locke, W. N. Martens, Synthesis and Raman spectroscopic characterisation of the oxalate mineral wheatleyite $Na_2Cu^{2+}(C_2O_4)\cdot 2H_2O$, J. Raman Spectrosc. 39 (2008) 901-908.

[25] R. L. Frost, M. L. Weier, Thermal treatment of weddellite – a Raman and infrared emission spectroscopic study, Thermochim. Acta 406 (2003) 221-232.

[26] D. M. Applin, M. R. M. Izawa, E. A. Cloutis, D. Goltz, J. R. Johnson, Oxalate minerals on Mars? Earth Planet. Sci. Lett. 420 (2015) 127–139.

[27] D. M. Applin, M. R. M. Izawa, E. A. Cloutis, Reflectance spectroscopy of oxalate minerals and relevance to Solar System carbon inventories, Icarus 278 (2016) 7–30.

[28] E. T. Peltzer, J. L. Bada, G. Schlesinger, S.L. Miller, The chemical conditions on the parent body of the Murchison meteorite: some conclusions based on amino, hydroxy and dicarboxylic acids, Adv. Space Res. 4 (1984) 69–74.

[29] A. Shimoyama, R. Shigematsu, Dicarboxylic acids in the Murchison and Yamato-791198 carbonaceous chondrites, Chem. Lett. 23 (1992) 60-62.

[30] a) S. Pizzarello, A. J. Garvie, Sutter's Mill dicarboxylic acids as possible tracers of parent-body alteration processes. Meteorit. Planet. Sci. 49 (2014) 2087–2094; b) S. Pizzarello, Y. Huang, L. Becker, R. J. Poreda, G. Cooper, M. Williams, The organic content of the Tagish Lake meteorite. Science 21 (2001) 2236–2239.

[31] B. Salvadori, V. Errico, M. Mauro, L. Dei, Evaluation of Gypsum and Calcium Oxalates in Deteriorated Mural Paintings by Quantitative FTIR Spectroscopy, Spectrosc. Lett. 36 (2003) 501-513

[32] I. Lamprecht, A. Reller, R. Riesen, H. G. Wiedemann, Ca-oxalate films and microbiological investigations of the influence of ancient pigments on the growth of lichens, J. Thermal Anal. 49 (1997) 1601-1607.

[33] A. Piterans, D. Indriksone, A. Spricis, Biodeterioration of stone historical monuments in Latvia, Proc. Latvian Acad. Sci. B 51 (1997) 254-260.

[34] M. Del Monte, C. Sabbioni, Weddellite on limestone in the Venice [Italy] environment, Environ. Sci. Technol. 17 (l983) 518-522.

[35] M. Del Monte, C. Sabbioni, Chemical and biological weathering of an historical building: Reggio Emilia Cathedral, Sci. Total Environ. 50 (l986) 165-182.

[36] H. G. M. Edwards, K. A. E. Edwards, D. W. Farwell, I. R. Lewis, M. R. D. Seaward, An approach to stone and fresco lichen biodeterioration through Fourier transform Raman microscopic investigation of thallus – substratum encrustation, J. Raman Spectrosc. 25 (1994) 99-103.

[37] H. G. M. Edwards, E, M. Newton, J. Russ, Raman spectroscopic analysis of pigments and substrata in prehistoric rock art, J. Mol. Struct. 550-551 (2000) 245-256.

[38] J. Girbal, J. L. Prada, R. Rocabayera, M. Argemi, Dating of biodeposits of oxalates at the Arc de Bera in Tarragona, Spain, Radiocarbon 43 (2001) 637-645.

[39] K. S. Alexander, D. Dollimore, J. G. Dunn, X. Gao, D. Patel, The determination of cholesterol, calcium carbonate and calcium oxalate in gallstones by thermogravimetry, Thermochim. Acta 215 (1993) 171-181.

[40] P. H. Chang, Y. H. Huang, C. L. Hsueh, M. C. Lu, G. H. Huang, Treatment of non-biodegradable wastewater by electro-Fenton method, Water Sci. Technol. 49 (2004) 213-218.

[41] A. Abd El-Raady, T. Nakajima, P. Kimchhayarasy, Catalytic ozonation of citric acid by metallic ions in aqueous solution, Ozone Sci. Eng. 27 (2005) 495-498.

[42] J. A. Zazo, J. A. Casas, A. F. Mohedano, M. A. Gilarranz, J. J. Rodriguez, Chemical pathway and kinetics of phenol oxidation by Fenton's reagent, Environ. Sci. Technol. 39 (2005) 9295-9302; W. C. Chu, C. Y. Kwan, K. H. Chan, S. K. Kam, A

study of kinetic modelling and reaction pathway of 2,4-dichlorophenol transformation by photo Fenton-like oxidation, J. Hazard. Mater. 121 (2005) 119-126.

[43] C.-H. Liu, Y.-H. Huang, H.-T. Chen, Study of oxalate mineralization using electrochemical oxidation technology, Environ. Eng. Manage. 17 (2007) 345-349.

[44] S. Budavari, M. O'Neil, A. Smith, eds., The Merck index; An encyclopedia of chemicals, drugs and biologicals, Merck Co. Inc., Rahway, 1989.

[45] M. Daudon, M. F. Protat, R. J. Reveillaud and H. Jaeschke-Boyer, Infrared spectrometry and Raman microprobe in the analysis of urinary calculi, Kidney Int. 23 (1983) 842-850.

[46] C. Paluszkiewicz, M. Galka, W. Kwiatek, A. Parczewski, S. Walas, Renal stone studies using vibrational spectroscopy and trace element analysis, Biospectrosc. 3 (1997) 403-407.

[47] E. C. Gruen, R. A. Plane, Raman study of aqueous metal oxalate complexes and related oxalates, Inorg. Chem. 6 (1967) 1123-1127.

[48] G. M. Begun and W. H. Fletcher, Vibrational spectra of aqueous oxalate ion, Spectrochim. Acta 19 (1963) 1343-1349.

[49] R. I. Bickley, H. G. M. Edwards, S. J. Rose, A Raman spectroscopic study of nickel(II) oxalate dihydrate, $NiC_2O_4 \cdot 2H_2O$ and dipotassium bisoxalatonickel(II) hexahydrate, $K_2Ni(C_2O_4)_2 \cdot 6H_2O$, J. Mol. Struct. 243 (1991) 341-350.

[50] H. Chang, P. J. Huang, Thermal decomposition of $CaC_2O_4 \cdot H_2O$ studied by thermo-Raman spectroscopy with TGA/DTA, Anal. Chem. 69 (1997) 1485-1491.

[51] T. A. Shippey, Vibrational studies of calcium oxalate monohydrate (whewellite) and an anhydrous phase of calcium oxalate, J. Mol. Struct. 63 (1980) 157-166.

[52] D. Duval and R. A. Condrate, Temperature Dependence of the Raman Spectra of Calcium Oxalate Monohydrate, Phys. Status Solidi B 132 (1985) 83-92.

[53] D. Duval and R. A. Condrate, A Raman Spectral Study of the Dehydration of Calcium Oxalate Monohydrate, Appl. Spectrosc. 42 (1988) 701-703.

[54] R. J. H. Clark, S. Firth, Raman, infrared and force field studies of $K_2{}^{12}C_2O_4 \cdot H_2O$ and $K_2{}^{13}C_2O_4 \cdot H_2O$ in the solid state and in aqueous solution, and of $(NH_4)_2\ {}^{12}C_2O_4 \cdot H2O$ and $(NH_4)_2\ {}^{13}C_2O_4 \cdot H_2O$, Spectrochim. Acta, A 58 (2002) 1731–1746.

[55] B. B. Parekh, P. M. Vyas, S. R. Vasant, M. J. Joshi, Thermal, FT–IR and dielectric studies of gel grown sodium oxalate single crystals, Bull. Mater. Sci. 31 (2008) 143–147.

[56] D. A. Reed, M. M. Olmstead, Sodium Oxalate Structure Refinement, Acta Crystallogr. B 37 (1981) 938–939.

[57] G. A. Jeffrey, G. S. Parry, The Crystal Structure of Sodium Oxalate, J. Am. Chem. Soc. 76 (1954) 5283-5286.

[58] E. V. Boldyreva, H. Ahsbahs, V. V. Chernyshev, S. N. Ivashevskaya, A. R. Oganov, Effect of hydrostatic pressure on the crystal structure of sodium oxalate: X-ray diffraction study and ab initio simulations, Z. Kristallogr. 221 (2006) 186–197.

[59] J. J. P. Stewart, Application of the PM6 method to modeling the solid state, J. Mol. Model. 14 (2008) 499–535.

[60] P. S. Lakkaraju, M. Askerka, H. Beyer, C. T. Ryan, T. Dobbins, C. Bennett, J. J. Kaczur, V. S. Batista, Formate to Oxalate: A Crucial Step for the Conversion of Carbon Dioxide into Multi-Carbon Compounds, ChemCatChem 8 (2016) 3453–3457.

[61] a) P. Hohenberg, W. Kohn, Inhomogeneous Electron Gas, Phys. Rev. 136 (1964) B864–B871; b) W. Kohn, L. J. Sham, Self-Consistent Equations Including Exchange and Correlation Effects, Phys. Rev. 140 (1965) A1133–A1138; c) R. G. Parr, W. Yang, Density-Functional Theory of Atoms and Molecules, Oxford University Press, New York, 1989.

[62] M. C. Payne, M. P. Teter, D. C. Ailan, A. Arias, J. D. Joannopoulos, Iterative Minimization Techniques for Ab Initio Total-Energy Calculations: Molecular Dynamics and Conjugate Gradients, Rev. Mod. Phys. 64 (1992) 1045–1097.

[63] L. J. Bonales, F. Colmenero, J. Cobos, V. Timón, Spectroscopic Raman Characterization of Rutherfordine: Combined DFT and Experimental Study, Phys. Chem. Chem. Phys. 18 (2016) 16575–16584.

[64] F. Colmenero, L. J. Bonales, J. Cobos, V. Timón, Study of the Thermal Stability of Studtite by In Situ Raman Spectroscopy and DFT Calculations, Spectrochim. Acta. A 174 (2017) 245–253.

[65] F. Colmenero, L. J. Bonales J. Cobos and V. Timón, Thermodynamic and mechanical properties of rutherfordine mineral based on density functional theory. J. Phys. Chem. C 121 (2017) 5994-6001.

[66] F. Colmenero, L. J. Bonales, J. Cobos and V. Timón, Structural, mechanical and vibrational study of uranyl silicate mineral soddyite by DFT calculations, J. Solid State Chem. 253 (2017) 249-257.

[67] F. Colmenero, L. J. Bonales, J. Cobos and V. Timón, Density Functional Theory Study of the Thermodynamic and Raman Vibrational Properties of $\gamma - UO_3$ Polymorph, J. Phys. Chem. C 121 (2017) 14507−14516.

[68] a) S. J. Clark, M. D. Segall, C. J. Pickard, P. J. Hasnip, M. I. J. Probert, K. Refson, M. C. Payne, First Principles Methods Using CASTEP, Z. Kristallogr. 220 (2005) 567–570; b) V. Milman, K. Refson, S. J. Clark, C. J. Pickard, J. R. Yates, S.-P. Gao, P. J. Hasnip, M. I. J. Probert, A. Perlov, M. D. Segall, Electron and Vibrational Spectroscopies Using DFT, Plane Waves and Pseudopotentials: CASTEP Implementation, J. Mol. Struct. THEOCHEM 954 (2010) 22–35.

[69] Materials Studio, http://accelrys.com/products/materials-studio, (2014).

[70] J. P. Perdew, K. Burke, M. Ernzerhof, Generalized Gradient Approximation Made Simple, Phys. Rev. Lett. 77 (1996) 3865–3868.

[71] S. Grimme, Semiempirical GGA-type Density Functional Constructed with a Long-Range Dispersion Correction, J. Comput. Chem. 27 (2006) 1787–1799.

[72] N. Troullier, J. L. Martins, Efficient Pseudopotentials for Plane-Wave Calculations, Phys. Rev. B 43 (1991) 1993–2006.

[73] B. G. Pfrommer, M. Cote, S. G. Louie, M. L. Cohen, Relaxation of Crystals with the Quasi-Newton Method, J. Comput. Phys. 131 (1997) 233–240.

[74] H. J. Monkhorst, J. D. Pack, Special Points for Brillonin-Zone Integration, Phys. Rev. B 13 (1976) 5188–5192.

[75] a) S. Baroni, S. de Gironcoli, A. Dal Corso, Phonons and Related Crystal Properties from Density-Functional Perturbation Theory, Rev. Mod. Phys. 73 (2001) 515–562; b) S. Baroni, P. Giannozzi, A. Testa, Green's-Function Approach to Linear Response in Solids, Phys. Rev. Lett. 58 (1987) 1861–1864.

[76] a) X. Gonze, D. C. Allan, M. P. Teter, Dielectric Tensor, Effective Charges and Phonon in α-Quartz by Variational Density-Functional Perturbation Theory, Phys. Rev. Lett. 68 (1992) 3603–3606; b) X. Gonze, C. Lee, Dynamical Matrices, Born Effective Charges, Dielectric Permittivity Tensors, and Interatomic Force Constants from Density-Functional Perturbation Theory, Phys. Rev. B 55 (1997) 10355–10368.

[77] K. Refson, P. R. Tulip, S. J. Clark, Variational Density-Functional Perturbation Theory for Dielectrics and Lattice Dynamics, Phys. Rev. B 73 (2006) 155114.

[78] W. J. Hehre, L. Radom, P. V. R. Schleyer, J. A. Pople, Ab Initio Molecular Orbital Theory, Wiley, New York, 1986.

[79] F. Colmenero, A. M. Fernández, J. Cobos, V. Timón, Thermodynamic Properties of Uranyl Containing Materials Based on Density Functional Theory, J. Phys. Chem. C 122 (2018) 5254−5267.

[80] F. Colmenero, A. M. Fernández, J. Cobos, V. Timón, Temperature Dependent Free Energies of Reaction of Uranyl Containing Materials Based on Density Functional Theory, J. Phys. Chem. C 122 (2018) 5268−5279.

[81] C. Lee, X. Gonze, Ab Initio Calculation of the Thermodynamic Properties and Atomic Temperature Factors of SiO2 α-Quartz and Stishovite. Phys. Rev. B 51 (1995) 8610–8613.

[82] M. W. Chase, C. A. Davies, J. R. Downey, D. J. Frurip, R. A. McDonald, A. N. Syverud, A. N. JANAF Thermochemical Tables. Third Edition. J. Phys. Chem. Ref. Data 14, Suppl. 1 (1985) 1–1856.

[83] D. Yu. Naumov, The application of structural analysis to the investigation of specific contacts in crystalline oxalates and their role in solid state decomposition. PhD. Thesis, Institute of Solid State Chemistry and Mechanochemistry, Siberian Branch of the Russian Academy of Sciences, Novosibirsk, Russia, 1997.

[84] A. P. Khomyakov, Natroxalate – $Na_2C_2O_4$ – a new mineral, Zap. Vses. Mineral. Obshch. 125 (1996) 126–132.

[85] H. E. Swanson, H. F. McMurdie, M. C. Morris, E. H. Evans, Standard X-ray diffraction powder patterns, Nat. Bur. Std. (US) Mon. 25-6 (1968) 70.

[86] R. T. Downs, K. L. Bartelmehs, G. V. Gibbs, M. B. Boisen, Interactive Software for Calculating and Displaying X-ray or Neutron Powder Diffractometer Patterns of Crystalline Materials, Am. Mineral. 78 (1993) 1104–1107.

[87] J. D. Martin, XPowder12, Ver. 04.13, 2012.

[88] ICDD, The International Center for Diffraction Data, PDF-2 Database, 2003.

[89] A. Tromans, E. Konigsberger, P. M. May, G. Hefter, Heat Capacities and Volumes of Aqueous Dicarboxylate Salt Solutions of Relevance to the Bayer Process, J. Chem. Eng. Data 50 (2005) 2019-2025; A. Tromans, Solution Chemistry of some dicarboxylate salts of relevance to the Bayer process. PhD. Thesis, Murdoch university, Western Australia, November 2003.

[90] S. L. Cherbov, E. L. Chernyak, Measurement of the specific heat of powdered aluminium oxide and sodium oxalate, Zh. Prykl. Khim. 10 (1937) 1220-1222.

[91] D. D. Wagman, W. H. Evans, V. B. Parker, R. H. Schumm, I. Halow, *et al.*, The NBS Tables of Chemical Thermodynamic Properties. Selected Values for Inorganic and C1 and C2 Organic Substances in SI Units. J. Phys. Chem. Ref. Data 11 Suppl. 2 (1992) 1–392.

[92] N. Chaiyo, R. Muanghlua, S., Niemcharoen, B. Boonchom, P. Seeharaj, N. Vittayakorn, Non-isothermal kinetics of the thermal decomposition of sodium oxalate, J. Therm. Anal. Calorim. 107 (2012) 1023–1029.

[93] M. J. John, K. Muraleedharan, M. P. Kannan, T. Ganga Devi, Kinetic studies on the thermal decomposition of phosphate-doped sodium oxalate, J. Therm. Anal. Calorim. 111 (2013) 137–144.

[94] T. Yoshimori, Y. Asano, Y. Toriumi, T. Shiota, Investigation on the drying and decomposition of sodium oxalate, Talanta 25 (1978) 603-605.